Crack growth and closure in cementitious composites: monitoring using piezoceramic sensors

Hussameldin M. Taha * [1][0000-0002-6167-7598], Richard J. Ball [1][0000-0002-7413-3944],

Andrew Heath [2] [0000-0003-0154-0941], and Kevin Paine [1][0000-0001-7455-7002]

1 BRE Centre for Innovative Construction Materials, Department of Architecture and Civil Engineering, University of Bath, Claverton Down BA2 7AY, United Kingdom.

2 Centre for Infrastructure, Geotechnical and Water Engineering Research (IGWE), Department of Architecture and Civil Engineering, University of Bath, Claverton Down BA2 7AY, United Kingdom.

1. Introduction:

The durable performance, easy shaping, availability of raw materials, and high compressive strength, makes concrete one of the most used materials in the construction industry [1]. However, the increased use of concrete in the built environment, comes with increasing greenhouse emissions and global anthropogenic CO_2 [2, 3]. Ensuring that our concrete structures are longer-lasting by improving durability and embedding autonomic self-healing technologies [4, 5] contributes significantly to reducing lifecycle emissions.

There are a number of self-healing technologies available for concrete. Some of these rely upon healing agents embedded in capsules or lightweight aggregates that open upon cracking of the concrete leading to almost automatic sealing of the crack over time [6, 7]. However, in other technologies, for example, flow networks [8] and shape-memory polymer technologies [9, 10], the healing is not automatic, and it relies upon observance of the damage and human intervention to trigger or release the healing mechanism [11,12]. If surveillance of the structure is not adequately observed then serious deterioration may occur despite the inclusion of self-healing technologies. This makes it necessary to develop reliable automated damage detection systems, which can detect incipient damage before activating these specific healing technologies.

Recently, piezoceramics, particularly lead zirconate titanate (PZT), have shown promise for damage detection and structural health monitoring in civil structures due to their sensitivity, fast response, and their low cost [13-16]. The use of piezoceramics in the electromechanical method, is advantageous since a single piezoceramic can be used as both a sensor and an actuator simultaneously [17, 18], which significantly reduces the sensing system's complexity.

In the electromechanical method, the relationship between the electrical admittance response, the inverse of the electrical impedance, collected from a surface attached or embedded PZT, and the structural mechanical impedance of a host structure, was derived by Liang, Sun [19] as shown in Equation (1)

$$Y = i\omega \frac{w_A l_A}{h_A} \left\{ \frac{d_{32}^2 \bar{Y}_{22}^E Z_A}{Z + Z_A} \frac{\tan k l_A}{k l_A} + \varepsilon_{33}^{-T} - d_{32}^2 \bar{Y}_{22}^E \right\} \quad (1)$$

Where:

- Y is the complex admittance
- $i = \sqrt{-1}$, ω is the excitation frequency
- w_A, l_A and h_A are the width, length and thickness of the PZT patch respectively
- $\bar{Y}_{22}^E$ is the complex modulus of the PZT patch at zero electrical field
- Z and Z_A are the mechanical impedance of the host structure and the PZT patch respectively
- $k = \sqrt{\frac{\omega^2 \rho}{\bar{Y}_{22}^E}}$
- ρ is the density of the PZT patch
- $d_{32}$the piezoelectric coefficient,
- ε_{33}^{-T} the complex electric permittivity in direction '3'at zero stress

Equation (1) suggests any changes in the mechanical properties of the host structure can be detected by collecting the electrical admittance/ impedance of the attached piezoceramic. As a result, the electromechanical method has been used to monitor the strength gain (hardening) and hydration process of concrete [20, 21]. Both hydration and hardening, affect the admittance signature by decreasing its value over time, particularly in specific effective frequency ranges, as well shifting the admittance signature resonance frequencies to higher frequency ranges [22-26].

Damage metrics and signal pattern recognition parameters have also been used to analyse the electrical response of PZT sensors. These included the root mean square deviation, RMSD,

correlation coefficient deviation, CCD, mean absolute percentage deviation, MAPD [27, 28], which are shown in Equations (2) to (5).

$$RMSD = \sqrt{\frac{\sum_{i=1}^{N}(y_i - x_i)^2}{\sum_{i}^{N}(x_i)^2}} \tag{2}$$

$$\mathrm{CCD} = 1 - \mathrm{CC} \tag{3}$$

$$CC = \frac{Cov(x, y)}{\sigma_x . \sigma_y} \tag{4}$$

$$MAPD = \frac{100}{N}\sum_{i=1}^{N}\left|\frac{y_i - x_i}{x_i}\right| \tag{5}$$

In which:

- $x_i \; and \; y_i$ are the real part of the admittance before and after the damage respectively.
- $\sigma_x \; and \; \sigma_y$ are the standard deviation for the signature before and after damage.
- $\bar{x}$ and $\bar{y}$ are the mean values of the signature before and after the damage.

These damage metrics have shown to be affected by the strength gain and the hydration process in cementitious composites [16, 29].

The mechanical loading effect on the electromechanical response has also been studied by subjecting cement paste samples to axial compression [30]. It was observed that the resonance peaks in both the thickness vibrational mode and the traverse mode, increased through three stages, in which these stages were correlated to the elastic, plastic, and fracture stages, respectively. Other studies which used surface attached PZT [31] and embedded ones [32] showed a decreasing trend in the resonance frequency as the stiffness degraded through loading for cementitious samples.

1.1 Research significance:

Despite the various studies that have focused on characterizing the electromechanical response of attached or embedded PZTs through different mechanical damage scenarios [33,34], the behaviour of the EMI response for cementitious composites under flexural loading and cracking needs more attention as many cementitious members in the field are damaged due to tension stresses in flexural loading scenarios. Furthermore, there is a scarcity of studies that addressed the effect of pre-peak loading /unloading and post-peak behaviour on the EMI response. In addition, and despite the increasing move to use self-healing and repair processes in cementitious materials, few studies have addressed the effect of these two processes on the electromechanical response [35, 36], although some studies have used PZT sensors through different other modes, such as the active mode, to detect healing and repair [37-39].

Considering that cracks in concrete propagate through the mortar phase [40], this study characterises the effect of flexural loading and cracking, ie, pre-peak and post-peak, on the electromechanical impedance approach by subjecting cement mortar samples to three-point bending scenario and then characterising the effect of stress-induced crack closure on PZT response. These two aspects of performance are needed to assess cracking and repair (crack closure) of concrete members in real operating conditions. Several researchers have used model materials (such as mortars) to allow results to be extrapolated to predict the behaviour of a related material (such as concrete). This practice has been used for applications such as characterisation of crack growth and crack healing, assessing the performance of steel corrosion inhibitors and tensile strength of mortars [40-43].

2. **Experimental programme:**

2.1 Samples preparation:

In this study, mortar specimens were used throughout the entire experimental programme.

The cement used was CEM I conforming to BS EN 197-1 [44], and the fine aggregate was standard sand conforming to BS EN 196-1 [45]. The water /cement ratio for all the samples was fixed at 0.5, and the sand to binder ratio used was 3.0.

The mixing was carried out in accordance with BS EN 196-1 [45]. Mortars were cast in 40 × 40 × 160 mm stainless steel moulds, and a total of four 40 × 40 × 160 mm mortar were cast, which are referred to hereafter as small-scale prisms.

A single unreinforced 500 ×100 × 100 mm mortar beam, which is referred to hereafter as 500 mm beam, was cast to support the results of the small-scale prisms. The former was made following the same mixing procedure mentioned above, however this time a wooden formwork and external poker vibrator were used in the casting.

After casting, the surfaces of the specimens were covered with cling film, and the specimens were demoulded after 24 hrs and then cured under water at 20 °C for 28 days. Thereafter, the specimens were transferred to a curing room of 21°C and 50% RH until required for further testing. 24 hours prior to testing, the top half of the small-scale prisms, compression zone, were wrapped with glass fibre sheet, which was glued to the side surfaces of the specimens by an epoxy agent, as shown in Figure 1 and Figure 2. This allowed for better crack width control through the experiment.

All the specimens were notched at the mid-span using a 2mm thick saw, and the notch depth was 1.5 mm and 5 mm for the small-scale prisms and the 500 mm beam, respectively.

Two 13mm diameter and 2mm thickness PIC 153 PZTs discs, with wrapped silver paint electrodes, see Figure 2 and Table 2 were surface attached to each specimen using Cyanoacrylate CN-Y adhesive from Tokyo measuring instruments labs. For the small-scale prisms, one of the PZTs was glued 30 mm from the centre, named PZT (C), and the other PZT, named PZT (S), was attached 80 mm from the centre of the prism. For the 500 mm beam, PZT (C) was attached 50 mm from the centre of the beam, and PZT (S) attached 250 mm from the centre of the beam, as shown in Figure 1-2 and Table 1

2.2 Experiment procedure:

2.2.1 Loading scenarios:

Two loading scenarios were followed through this study: (a) a three-point bending scenario to induce cracking, this was applied on all the samples, and (b) a compressive loading scenario to simulate crack recovery via, for example, a shape-memory polymer healing system [10], this was applied on one small-scale sample after inducing a crack by three-point bending.

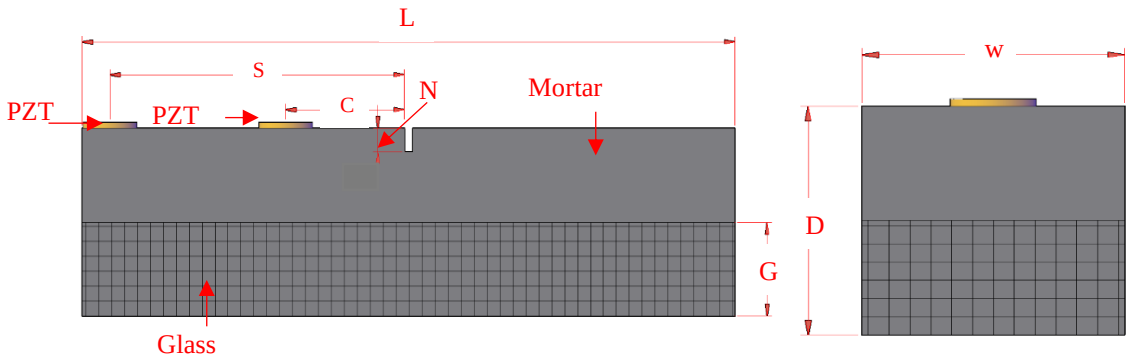

Figure 1: A schematic drawing for the mortar samples used through the study with dimensions shown in table (1).

Table 1: Dimensions of the mortar samples used in this study, as shown in Figure 1. All dimensions are in mm.

Sample Number	w	D	L	C	S	N	G
Small-scale prisms samples	40	40	160	30	80	1.5	20
500 mm beam sample	100	100	500	50	250	5	-

2.2.1.1 Three-point bending:

Three small-scale prism samples, named hereafter samples 1, 2 and 3, and the 500 mm mortar beam, hereafter named sample 4, were subjected to a series of three point-bending loading regimes. These involved sequential static loading and unloading, as shown in Figure 3. In addition, another small-scale sample, sample 5, was also pre-cracked using the same three-point bending method, which was later used in the crack-closure experiment, as discussed in Section 2.2.1.2.

Loads were applied using a 100 kN Instron static testing frame. Specimens were loaded over a span of 100 mm for samples 1 to 3, and 400 mm for sample 4, with the load applied at the centre of the specimens as shown in Figure 2. Specimens were supported on roller supports in accordance with BS EN 196-1 [42]. The loading on each sample was stopped after reaching a given crack width, ranging from 0.1 mm to 0.4 mm. These were measured using a UB-5A clip-shape crack mouth opening displacement (CMOD) gauge, from Techni Measure/ UK, which was attached to the bottom of the samples through glued perspex clips, as shown in Figure 2. The different loading regimes shown in Figure 3, which comprised of sequential static loading applied on sample 1 as shown in Figure 3 (a), and quasi-static cyclic loading applied on samples

2, 3 and 4 as shown in Figure 3 (b)-(d), were all selected to highlight the effect of loading, unloading, incipient damage and crack width on the electromechanical response of the PZT sensors. The force, displacement and the crack mouth opening were all monitored through the experiment for the small-scale samples, i.e., samples 1, 2 and 3, whilst only the force and displacement were monitored for the 500 mm beam sample, i.e.: sample 4.

A displacement-controlled mode was followed with a displacement rate of 0.05 mm/min during the experiment as the displacement control limited uncontrolled changes in the crack width.

2.2.1.2 Compressive loading scenario:

After being cracked in three-point bending, sample 5 was subjected to compressive loading to generate crack closure as shown in Figure 2 (e). Both the displacement and the crack mouth opening were measured during the compressive loading application. The compressive loading was conducted in a displacement-controlled mode with a displacement rate of 0.1 mm/min. Loading was stopped once signs of compressive damage, i.e. spalling, were visible.

Throughout both the three-point bending and the compressive loading, the impedance signature of the PZT sensors was collected at discrete loading points.

During the three-point bending, i.e. for samples 1, 2, 3 and 4, the loading and PZT reading points are shown in Figure 3. For the compressive loading experiment, the PZT response was collected first before cracking, ie: at the pristine stage before the three-point bending scenario was applied. The PZT response was collected again after cracking the sample in the three points bending loading scenario, and finally, the PZT response was collected through the compressive loading scenario at every 3 kN (1.9 MPa). In this case, only the impedance response for the near crack, ie PZT (C) was collected.

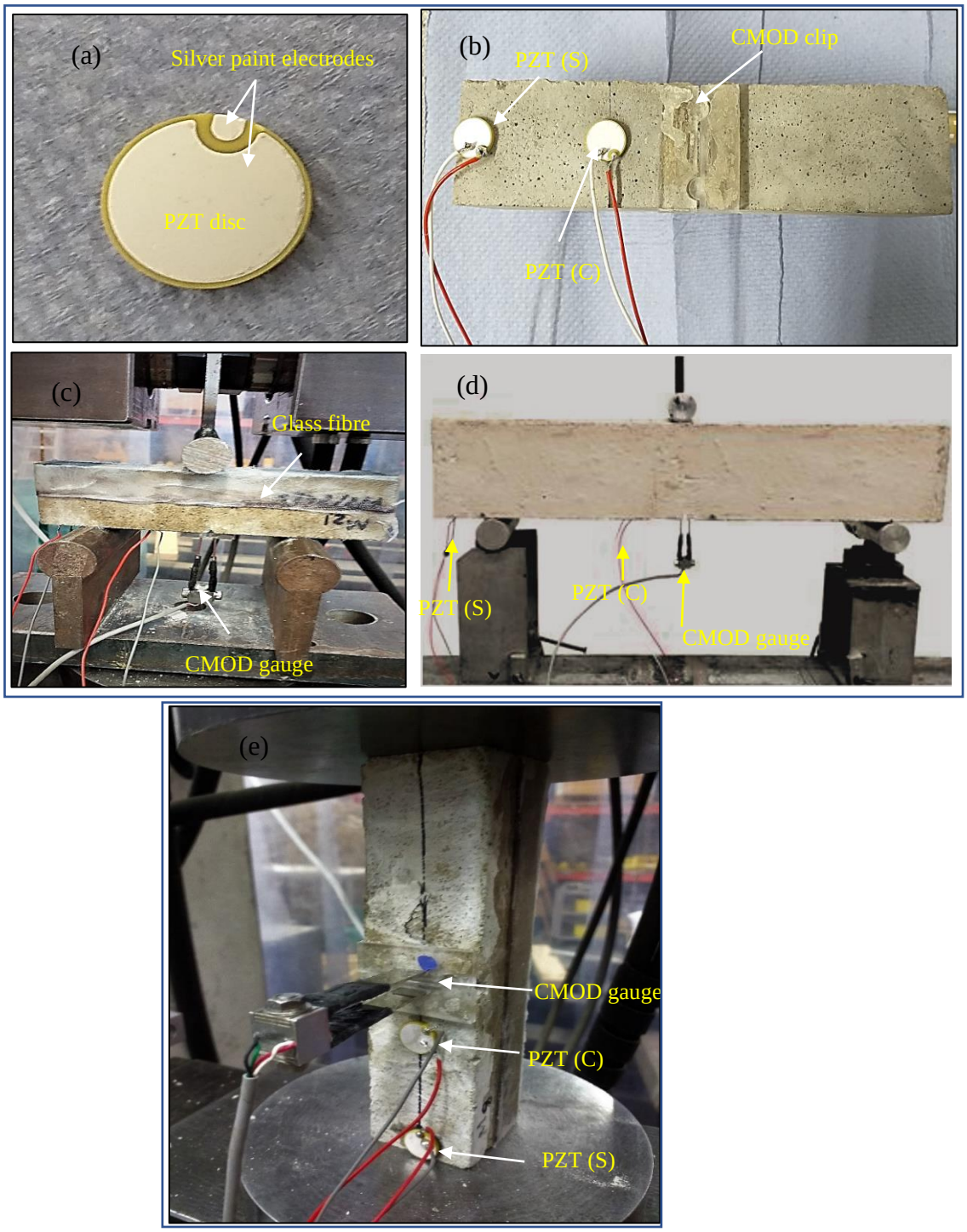

Figure 2: (a) PZT disc, (b) Attached PZT discs to a small-scale prism, (c) Three-point bending for small-scale prism specimen, (d) Three-point bending for 500 mm beam specimen, (e) compressive loading for pre-cracked small-scale mortar prism specimen.

Table 2: Properties of PZT material [46]

Property	**Value**
Material type	PIC 153
Density, (g/cm^3)	7.60
Electric Permittivity, $\varepsilon_{33}^T/\varepsilon_0$	4200
Piezoelectric Strain Coefficient, d_{33}(10^{-12} C/N)	600
Elastic Compliance Coefficient, S_{11}^E(10^{-12} m^2/N)	1960
Dielectric Loss Factor, tanδ (10^{-3})	30

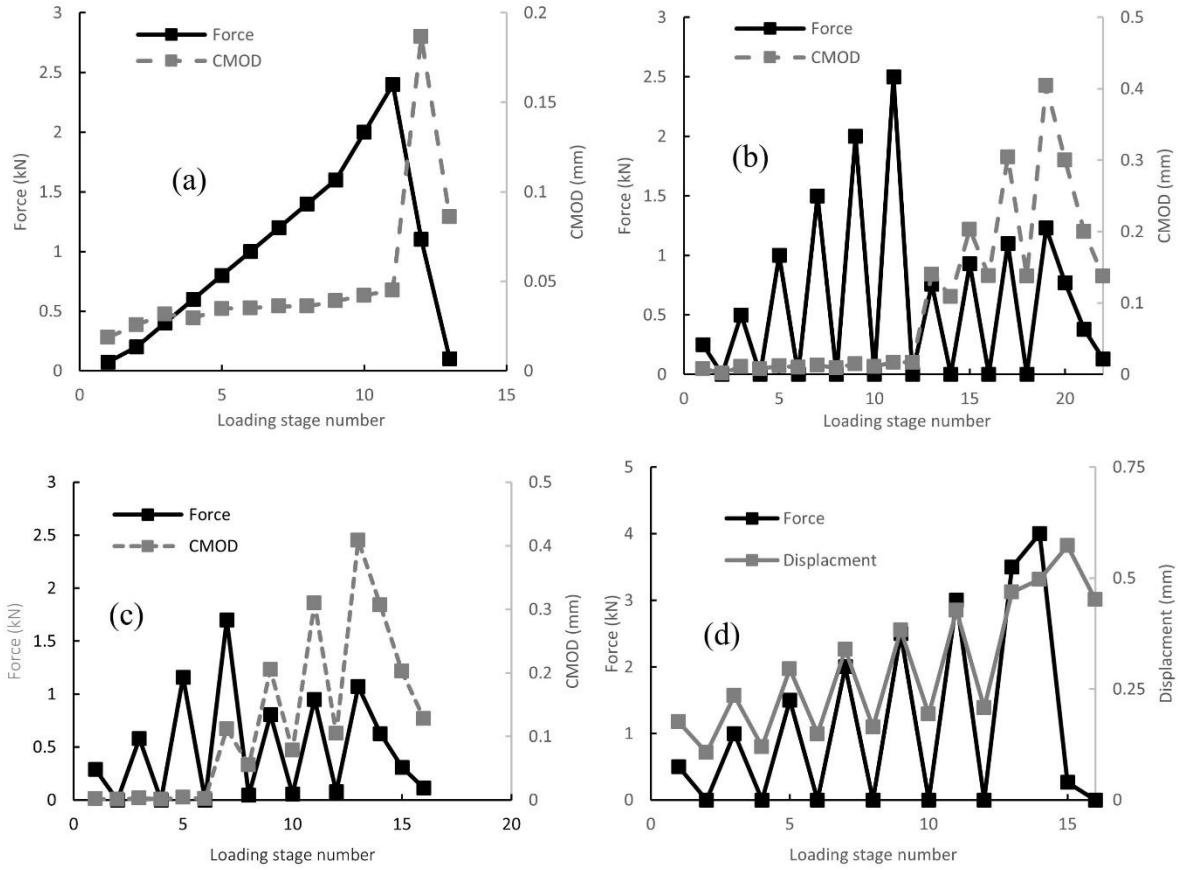

Figure 3: Followed loading regimes during the three-point loading experiment for the three representative small-scale prisms (a) sample 1, (b) sample 2 and (c) sample 3. And for the 500mm beam at (d) sample 4.

2.2.2 Electromechanical measurements:

The impedance response of the PZT sensors was collected with a Newtons4th PSM 3750 frequency analyser (Newtons4th Ltd., Leicester, UK) interfaced with an impedance analyser. The impedance analyser was connected to the PZT sensors through 50 Ω coaxial cables, which were connected at one end to the impedance analyser, and the other end connected to the wires which were soldered to the PZT sensors. The voltage used to actuate the PZT sensors was 2 V, and the impedance signature was collected in the frequency range of 15 – 350 kHz. 1000 points were collected in each sweep.

3. **Results and discussion:**

3.1 Impedance signature response:

Figure 4 shows the impedance signatures of PZT (C) sensor, for sample 2 during three-point bending, collected at the pristine, 0.25 kN (0.59 MPa), 0.5 kN (1.17 MPa), 1 kN (2.34 MPa), 2 kN (4.69 MPa) and the cracked stage. Defined impedance signature peaks were observed through the different frequency ranges, numbered P1- to P10, as shown in Figure 4.

It was observed that, as the loading increased, P1, P2 and P3, shifted to the right-hand side, showing an increase in their peak frequencies. This increasing trend for these peaks was also observed for the other peaks, although the phenomenon was most clear at lower frequency peaks, as shown in Table 3. This sensitivity to loading can also be seen in Figure 5 (a), where it was noticeable that as the measuring frequency increased, the peaks' frequencies tended to be less sensitive to the applied loading on the sample.

This increasing trend showed by the impedance signature peaks' frequencies in conjunction with the applied load, demonstrated the sensitivity of the impedance signature to the increase in the tensile stress at the tension zone, i.e. the bottom half of the hosting member. Hence the

impedance signature was capable of reflecting the increase in the hosting member natural frequency due to the applied tensile stress indirectly, by exhibiting an increase in the impedance signature peaks' frequencies [47, 48]

On the other hand, the decrease in the sensitivity of the impedance signature to the applied stress as the measuring frequency increased was due to the actuation localization effect at higher frequency ranges, hence the gradual domination of the PZT resonance/anti-resonance peak on the structural frequency peaks [49, 50]

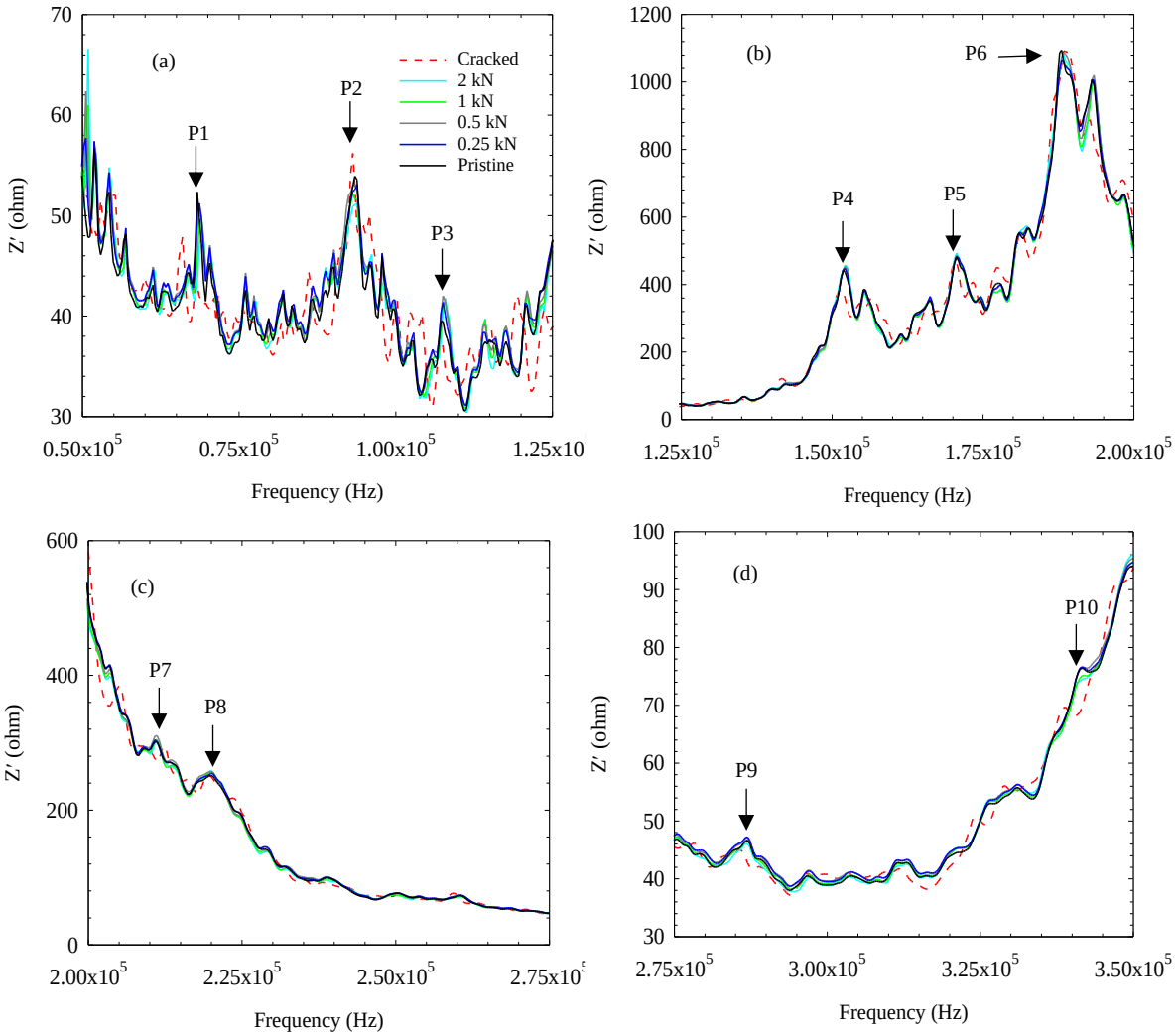

Figure 4: Impedance signature response for near-centre PZT disc, PZT(C), collected at different loading values in a three-points bending experiment for sample 2.

Once cracking initiated, an observed shift in the peaks' behaviour towards lower frequency ranges occurred, i.e., to the left-hand side (see Table 3 and Figure 4), which was attributed to the decrease in both the stiffness and the natural frequency of the specimen.

It is worth mentioning despite the evident shift in the peaks' frequencies to lower frequency ranges at the cracking stage, the shift might have different values at lower and higher frequency ranges, as the material mechanical properties, in this case, changed from the elastic state to the plastic.

In this case, it was noticeable that the higher frequency peaks at the cracking stage, were also affected by the crack occurrence, as demonstrated by peaks number P8, P9 and P10 in Figure 5 (a) and Table 3.

In terms of the impedance signature amplitude response, Figure 5 (b) shows the normalised impedance amplitude with respect to the pristine stage for each peak through different loading stages. In general, the amplitude response for the different peaks did not follow a consistent trend; however, despite this the impedance amplitude changes with loading on the samples. In addition, it was noteworthy that the low-frequency peak amplitudes were more affected by the loading than the higher frequency amplitudes. This was observed by considering the percentage difference between the pristine stage impedance signature and the 2 kN loading stage for P1, P2, P3, as the difference recorded 8%, 5% 5.8%, respectively, whereas for P4, P6, P8, P9 and P10 it recorded 3.3%, 2%, 1%, 0.3%, 1% and 3%, respectively.

Table 3: Impedance signature peaks frequency (kHz), through different loading stages.

	Loading stage					
Peak number	Pristine	0.25 kN (0.59 MPa)	0.5 kN (1.17 MPa)	1 kN (2.34 MPa)	2 kN (4.69 MPa)	cracked
P1	68.294	68.684	68.684	69.010	69.075	65.971
P2	93.469	93.804	93.804	93.133	93.804	93.133
P3	107.220	107.550	107.550	107.890	107.890	107.220
P4	151.820	152.150	152.150	152.150	152.150	151.480
P6	188.030	188.030	188.370	188.030	188.370	186.690
P8	219.890	220.230	219.890	219.890	219.890	219.560
P9	286.960	286.960	286.960	286.960	286.620	285.620
P10	341.620	341.620	341.620	341.950	341.620	338.930

After cracking, the impedance amplitude for the peaks shown in Figure 5 (b), showed a decreasing tendency which was noticeable when assessing the peaks' normalised impedance amplitude.

3.2 First difference Impedance signature response:

The changes in the electromechanical response of the PZT sensor can also be assessed by assessing the changes in the first difference of the impedance signature, *d(Z)*. The advantage of this method is to detrend the impedance signature response, hence unveiling local peaks which are masked by adjacent maximum global peaks.

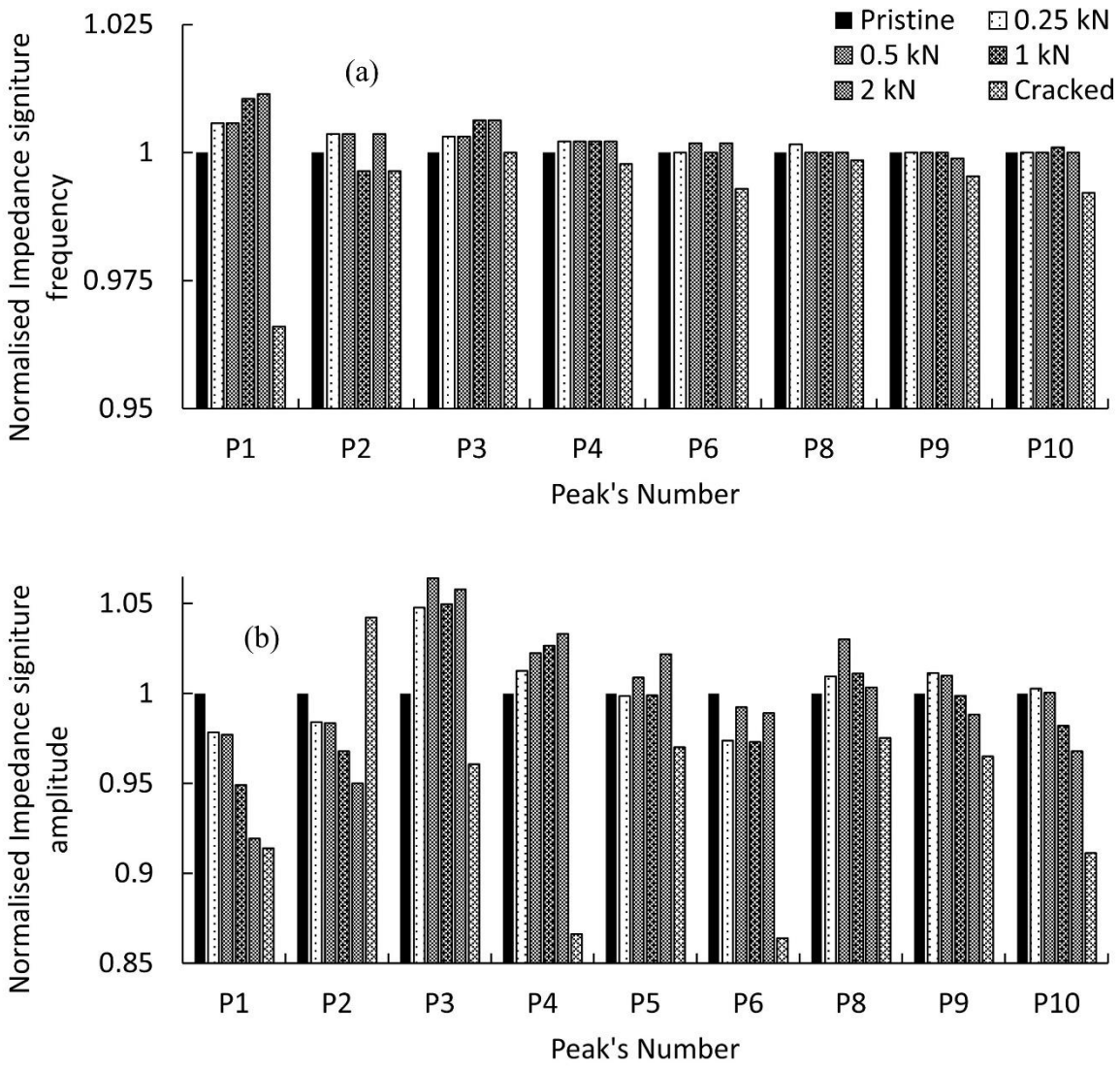

. Figure 5: (a) Normalised Impedance signature peaks frequencies, and amplitudes (b), through different loading stages. Legend is shown in (a).

Figure 6 shows the absolute values for the first difference impedance signature $|d(Z)|$ for the pristine, 0.25 kN, 0.5 kN, 1 kN, 2 kN, and the cracked stage for PZT (C). To further assess the $d(Z)$ response at different loading stages, Figure 7 shows the $|d(Z)|$ response at: the pristine stage, the 2 kN (4.688 MPa) and the cracked stage. In this case, and due to the high peaks density observed on the $|d(Z)|$ plot, the effect of loading was assessed exclusively on the highest $|d(Z)|$ peak, which occurred at 187 kHz. In this main peak, the pristine stage amplitude recorded the highest value compared to the other two loading stages.

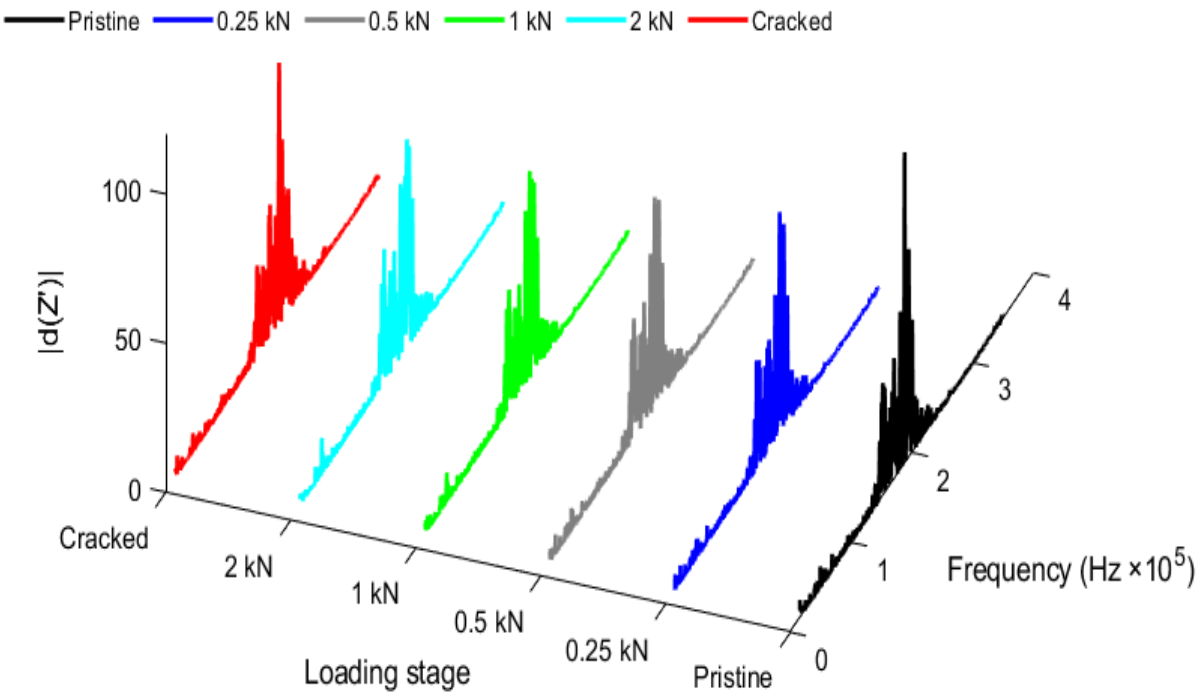

Figure 6: The absolute value of the first difference impedance signature |*d(Z)*| through different loading stages in the frequency range of 15 kHz - 350 kHz.

Despite this decrease in |*d(Z)*| main peak when increasing the loading to 2 kN, an increase in the |*d(Z)*| amplitude occurred once the sample cracked. A shift in this maximum peak to lower frequency ranges was also observed once the sample cracked, as the values of 187 kHz, 187.360 kHz and 185.690 kHz were recorded for the pristine, 2 kHz and the cracked stage, respectively. Also, it was observed that the |*d(Z)*| amplitude responded differently at different measuring frequencies.

To assess the sensitivity of both the *Z* and the *d(Z)* for the effect of loading and cracking in the sample, Figure 8 (a) and (b) show the variation in the impedance signature and the first difference impedance signature for the 0.25 kN (0.59 MPa), 0.5 kN (1.17 MPa), 1 kN (2.34 MPa), 2 kN (4.69 MPa) and the cracking stage, when plotted against their respective pristine stages.

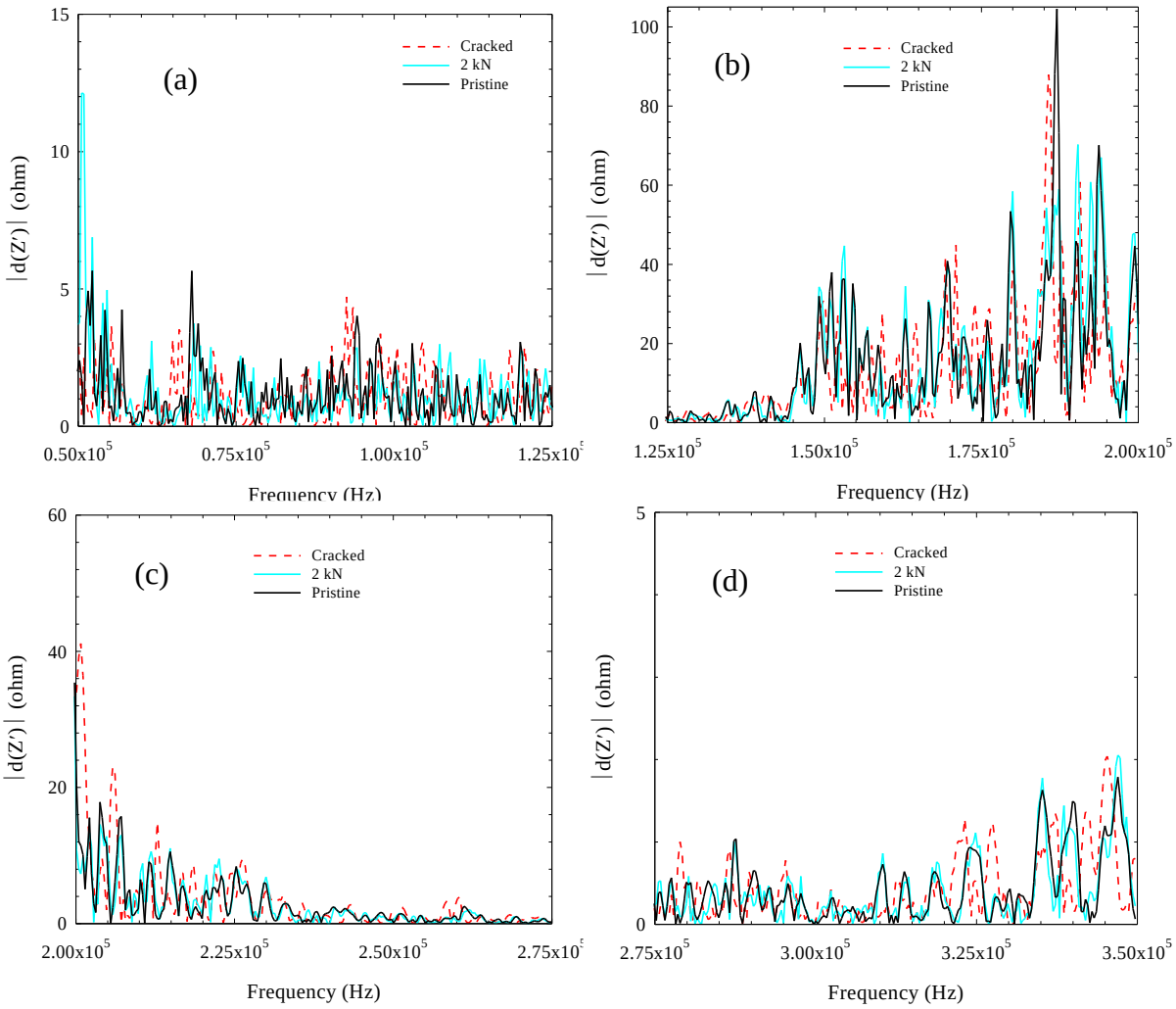

Figure 7: The absolute value of the first difference impedance signature response $|d(Z)|$ at the pristine, 2kN and the cracked stages shown at the frequency ranges of: (a) 50-125 kHz, (b) 125 kHz-200 kHz, (c) 200- 275 kHz (c) 275-350 kHz.

By assessing the R^2 values for the different damage stages shown in Figure 8, the cracking stage for both the impedance signature *(Z)* and the first difference impedance signature *d(Z)*, recorded the lowest R^2 values, and the 0.25 kN recorded the highest value as shown in Table 4. It was also evident that the *d(Z)* based R^2 values, record lower values than the *Z* based R^2 values, suggesting that the *d(Z)* response was more sensitive to the loading and the cracking process.

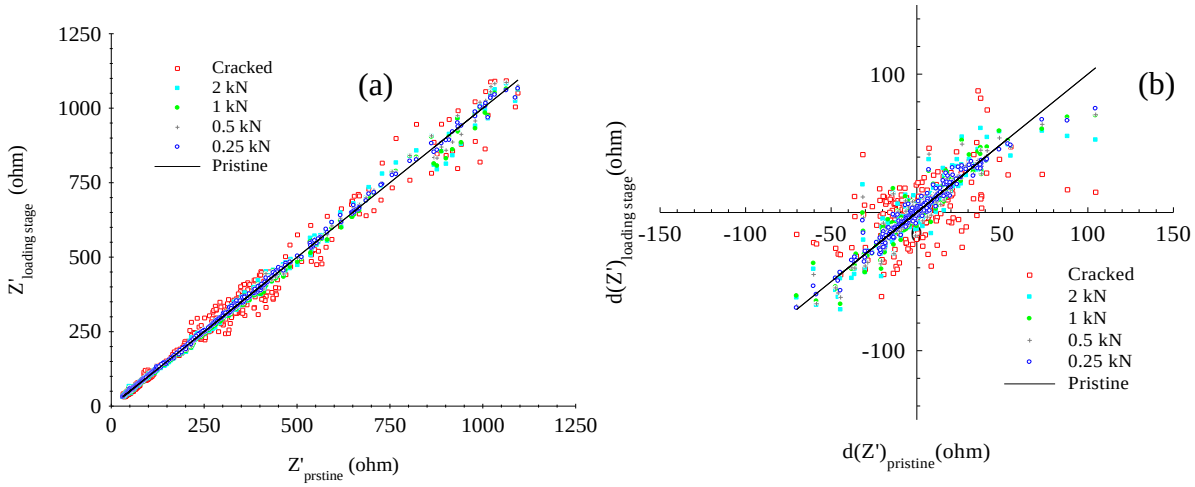

Figure 8: (a) The pristine stage impedance signature $Z_{prstine}$ versus different loading stages impedance signatures, (b): The first difference pristine stage impedance signature $d(Z)_{prstine}$ versus different first difference impedance signature loading stages.

Table 4: R^2 values for the relationship between the signatures for both pristine and loaded stages; calculated based on the impedance signature Z and the first difference of the impedance signature $d(Z)$

Loading stage	R^2_Z	R^2_{dZ}
0.25 kN (0.59 MPa)	0.999	0.942
0.5 kN (1.17 MPa)	0.998	0.895
1 kN (2.34 MPa)	0.998	0.889
2 kN (4.69 MPa)	0.997	0.826
Cracked	0.988	0.279

3.3 *Z*-based and *dZ*-based damage metrics responses:

In this study, a modified version of the R^2 parameter, *Rmod*, was used to quantify the change in the impedance signature.

Rmod was calculated as:

$$Rmod = (1 - R^2) \times 100 \quad (6)$$

The *Rmod* parameter in this study was either impedance signature-based estimated named *Rmod (Z)*, or first difference impedance-based estimated, named *Rmod (dZ)*.

In Figure 9, the *Rmod* responses of the near centre sensor denoted as PZT (C), and the near support sensor, denoted as PZT (S), were assessed and are shown for sample 1, in Figure 9 (a) and (a`), and for sample 2 in Figure 9 (b) and (b`). In Figure 9, both the *Rmod (Z)* and the *Rmod (dZ)* were assessed in the frequency interval of 65 – 115 kHz.

Regarding the *Rmod (Z)* response before cracking for PZT (C) in Figure 9 (a), this damage metric increases continuously with the continuous loading regime followed in sample 1. After cracking, an abrupt increase in the *Rmod (Z)* values is noticed, which was unrecoverable even after unloading the sample.

For sample 2, which is shown in Figure 9 (b), it is evident that the *Rmod (Z)* for PZT (C) fluctuates following the loading and the unloading regime. This behaviour indicates that the response of the sensors before cracking is recoverable once the load has been removed. After cracking, again, an abrupt increase in the *Rmod (Z)* was evident, as was the case in all specimens.

By considering the first difference impedance-based damage metric response, *Rmod (dZ)*, which is shown in Figure 9 (a`) and (b`), this parameter showed considerably higher values compared with the impedance-based *Rmod (Z)* both before cracking and after cracking. These high values for the *Rmod (dZ)* in comparison to the *Rmod (Z)* before and after cracking stages, support the high deviation result from the pristine stage, which was observed in both Figure 8 and Table 4.

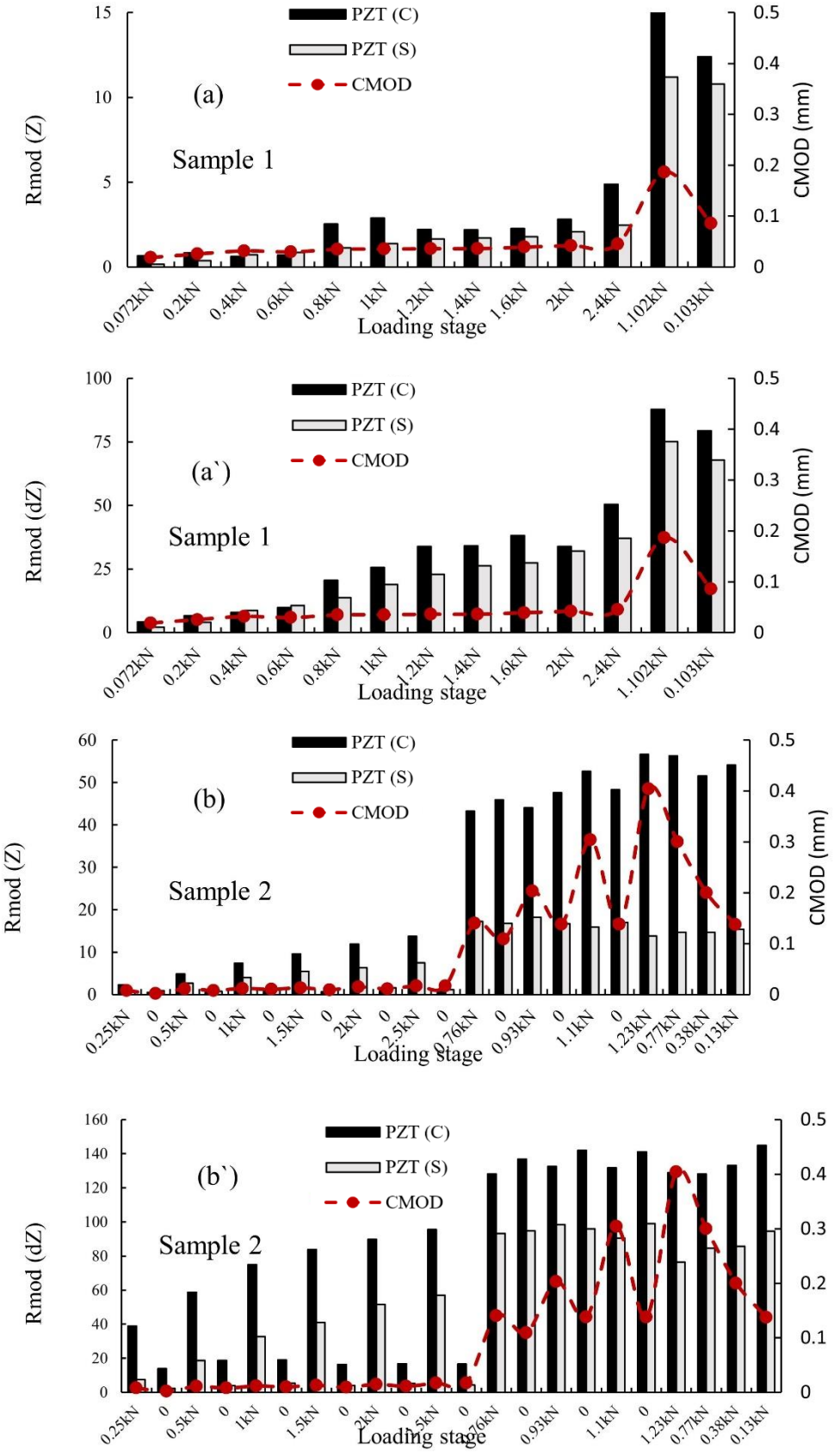

Figure 9: *Rmod* damage metric response for the near centre, PZT (C), and the near support PZT (S) sensors, shown for sample 1 at (a), and (a`) and for sample 2 at (b) and (b`).

3.4 Relation between *d(Z)* and *Z* based damage metrics.

Figure 10 (a), (b) and (c) show the relationship between the *Rmod (Z)* and the *Rmod (dZ)* for PZT (C) sensors, for samples 1, 2 and 3. The observed non-linear sigmoidal relationship between the *Rmod (Z)* and *(dZ),* indicates the relationship changes as the samples pass through different loading stages. By considering Figure 10 (b) as an example, at lower values, < 10 and < 50 for both the *Rmod (Z)* and the *Rmod (dZ),* respectively, the relationship was almost linear. However, as both the *Rmod (Z)* and the *Rmod (dZ)* values increased, the relationship started to deviate from linearity. After cracking, the *Rmod (Z)* and *Rmod (dZ)* values clustered at narrow range, indicating that these two parameters started to become less sensitive to loading.

The deviation from linearity suggests that a gradual change in the mechanical properties was taking place throughout loading which can be explained in terms of a gradual loss of stiffness due to the formation of microcracks before reaching the peak load [41, 51]. After cracking, due to the decrease in the sample stress/ strain transmission capability, which depended on the crack width [52], the sensors did not detect further changes in the sample.

3.5 Effect of electrical frequency range on the sensing capability of PZT sensors:

Figure 11-Figure 14 show the responses of PZT (C) and PZT (S) for samples 1, 2 and 3. Seven frequency bands of 50 kHz intervals were used to estimate the *Rmod (Z)* and the *Rmod (dZ)* behaviours through the various loading stages. These seven frequency bands are shown on the y-axis at the left-hand side. All the colour mapped values shown for both the *Rmod (Z)* and *Rmod (dZ),* are fractional percentages with respect to the maximum value recorded through the entire frequency range for each PZT sensor.

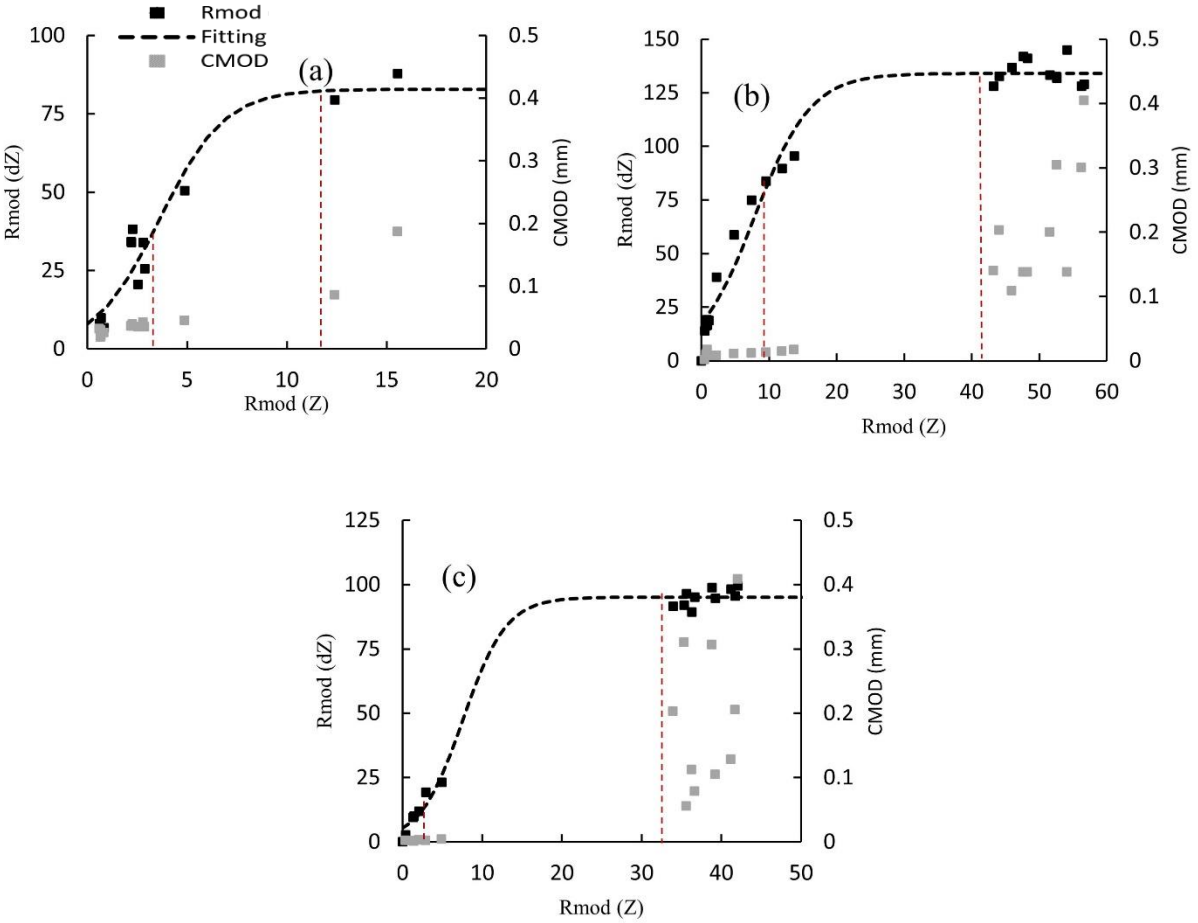

Figure 10: Relation between the impedance based and the first difference impedance based damage metrics for PZT (C) in (a) sample 1, (b) sample 2 and (C) sample 3. Legend is shown in (a).

From Figure 11-Figure 14, and by considering the response of both PZT (C) and PZT (S), it was evident that more frequency bands in the *Rmod (dZ)* response were affected by the loading and cracking when compared with the *Rmod (Z)* response, especially after the cracking stage. This finding highlights the importance of data detrending when analysing the electromechanical response for damage detection purposes.

When considering the effect of sensor distance from the damage on the *Rmod (Z)* responses at different frequency bands, it was evident that as the distance between the sensor and the damage increased, the lower frequency bands become more sensitive, especially at the post-damage stage.

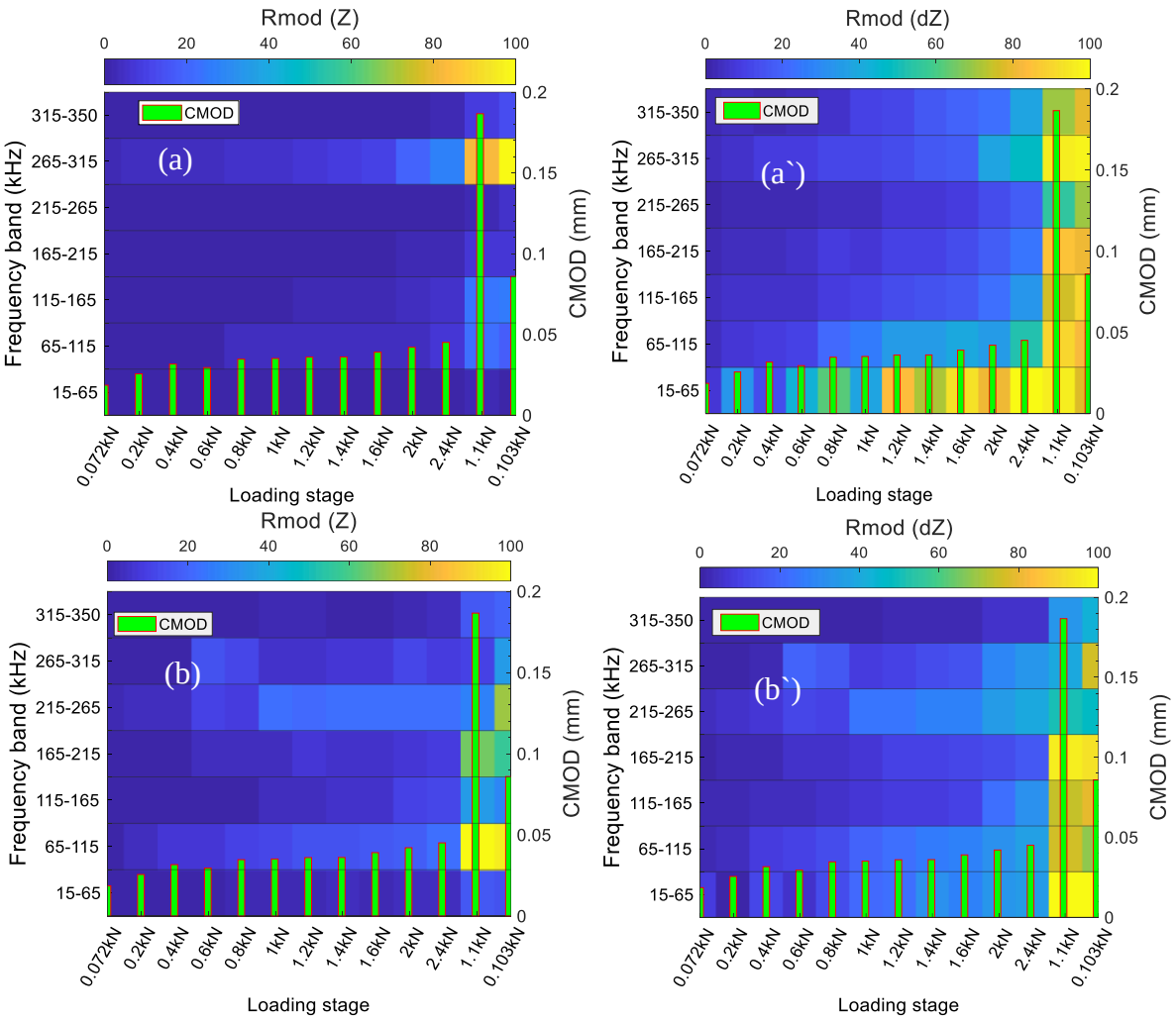

Figure 11: Sample 1 *Rmod (Z)* and *Rmod (dZ)* responses, estimated through different frequency intervals, for PZT (C) shown at (a) and (a') ,and PZT (S) shown at (b) and (b').

This behaviour can be demonstrated by considering sample 1 in Figure 11(a) and (b). For the post-damage response for PZT (C), the 265-315 kHz frequency band showed the highest sensitivity for cracking among the different frequency bands. On the other hand, for PZT (S), the 65-115 kHz frequency band showed the highest sensitivity to damage. This indicates a shift in the sensitive frequency bands to lower frequency ranges as the distance between the damage and the sensor increased.

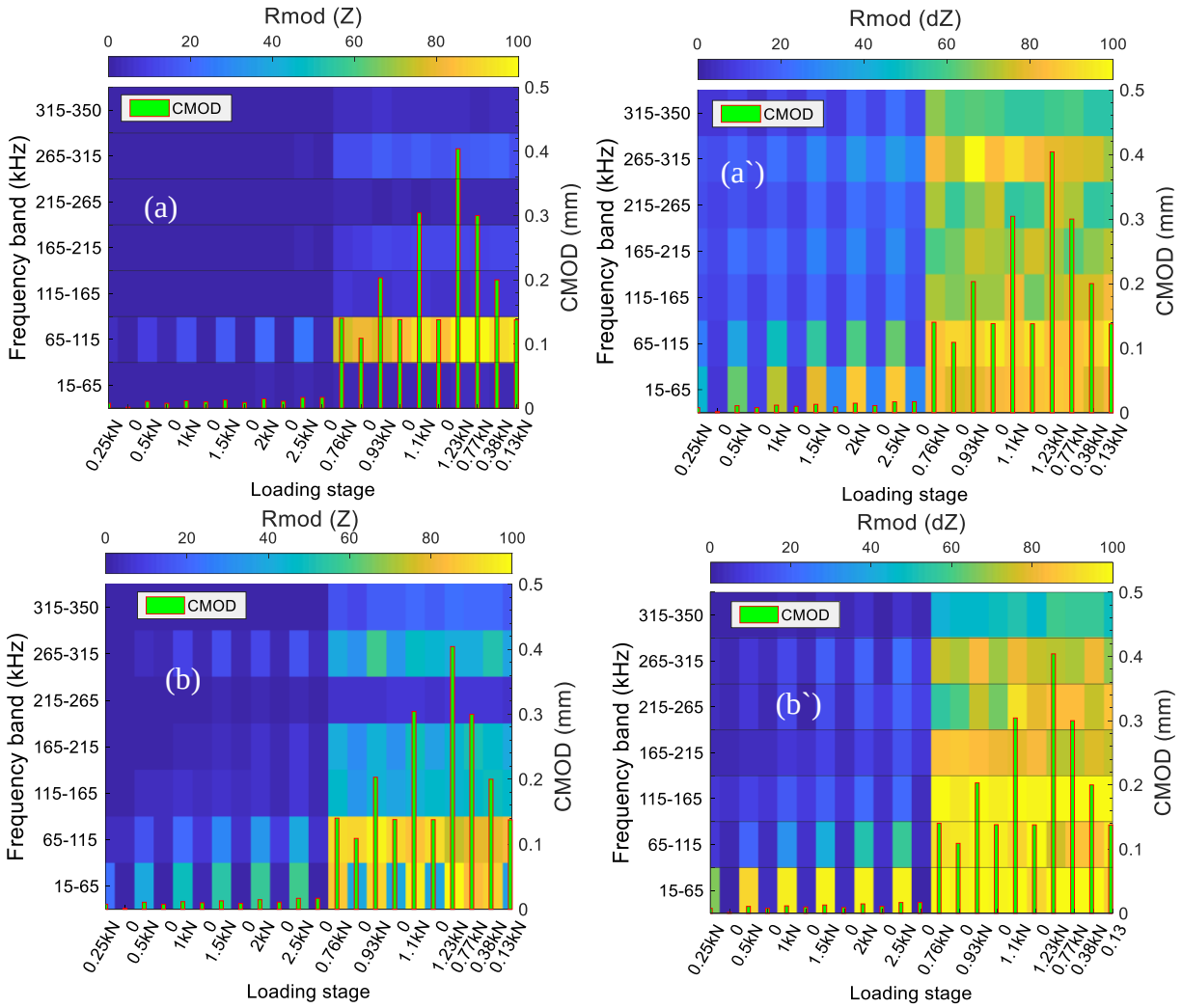

Figure 12: Sample 2 *Rmod(Z)* and *Rmod (dZ)* responses, estimated through different frequency bands, for PZT (C) shown at (a) and (a') ,and PZT (S) shown at (b) and (b').

Furthermore, with respect to the *Rmod (dZ)* behaviour after cracking, it was evident that higher frequency bands were more affected by damage in sensors that were closer to the damage, i.e. PZT (C), which is illustrated in sample 3 (Figure 13). This trend was also noticeable on the other two samples.

To further investigate the effect of distance between the damage and sensors, a supporting experiment using sample 4 (the 500 mm × 100 mm × 100 mm mortar beam) was conducted.

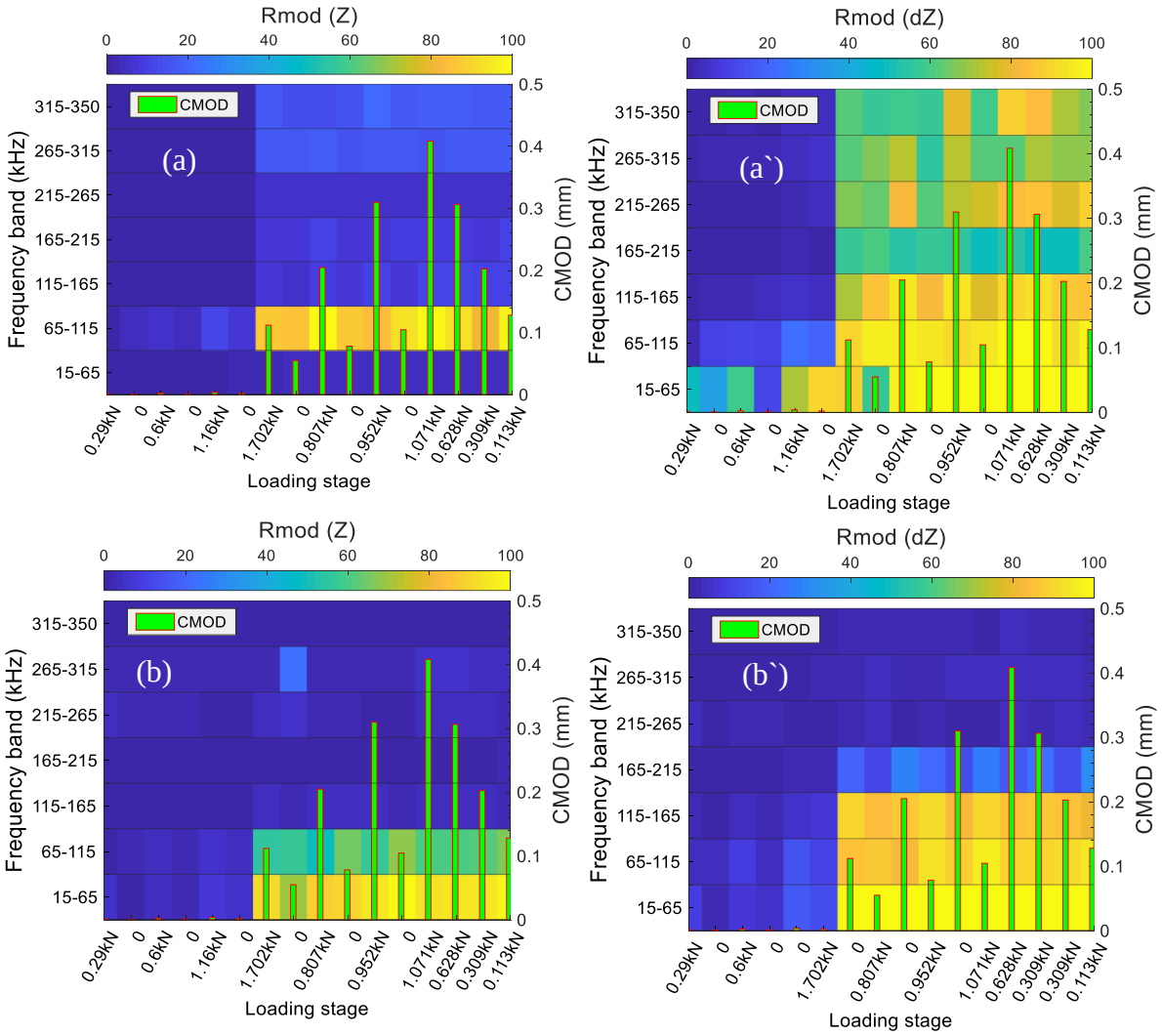

Figure 13: Sample 3 *Rmod (Z)* and *Rmod (dZ)* responses, estimated through different frequency intervals, for PZT (C) shown at (a) and (a') ,and PZT (S) shown at (b) and (b').

From Figure 14, it is demonstrated that as the distance between the sensor and the damage increased, the low-frequency bands become more sensitive to both damage and loading in the samples and vice versa as shown before on the results of the prismatic samples.

These results suggest cracking affected the high-frequency ranges of the impedance signature for the sensors closer to damage; however, for sensors further from the damage, the sensitive frequency band shifted to lower frequency ranges.

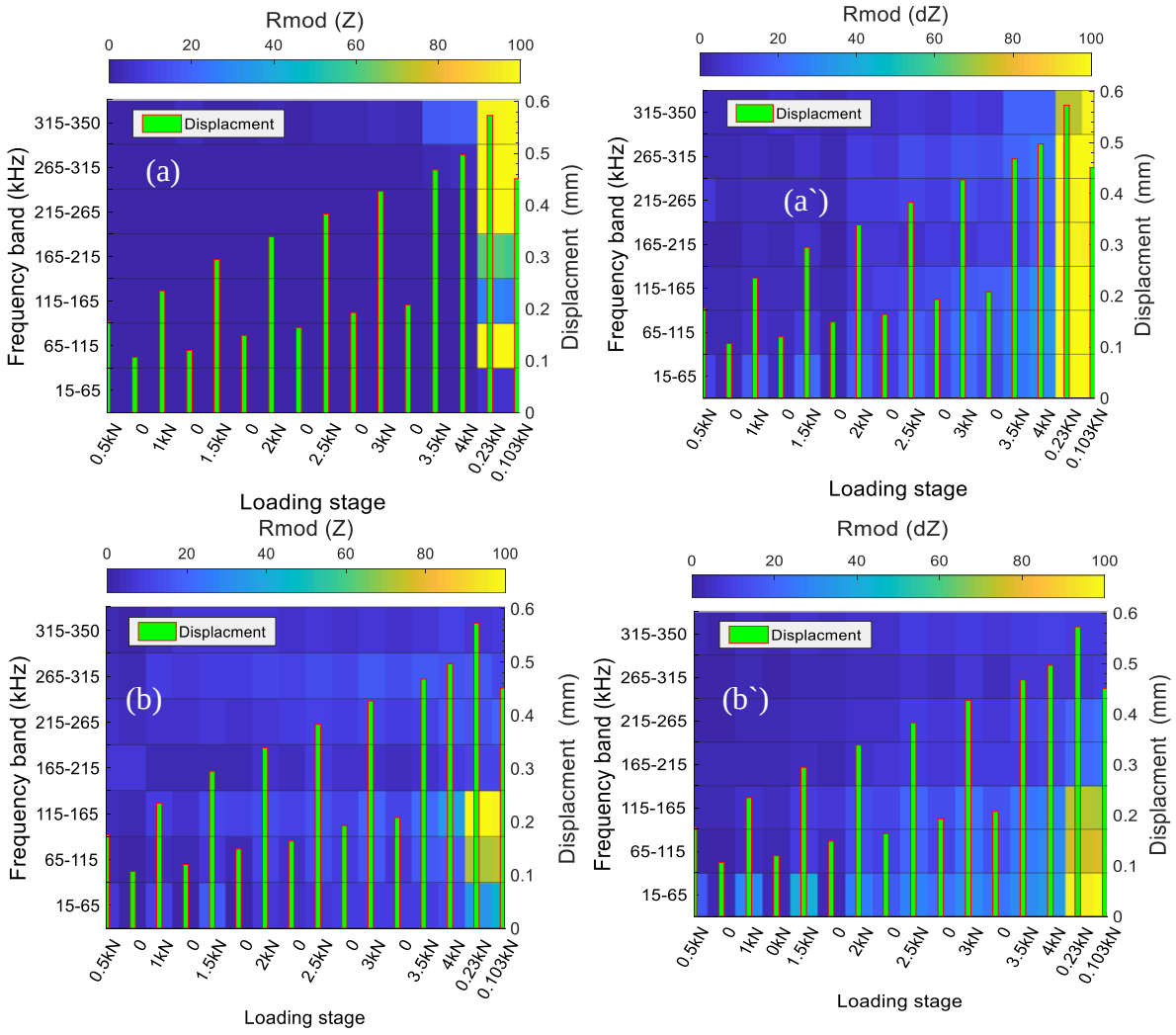

Figure 14: Sample 4 *Rmod (Z)* and *Rmod (dZ)* responses, estimated through different frequency intervals, for PZT (C) shown at (a) and (a') ,and PZT(S) shown at (b) and (b').

3.6 Effect of crack closure on pre-cracked samples:

In this section, the effect of crack closure due to the application of compressive loading for a pre-cracked sample, i.e., sample 5, was assessed through the electromechanical response of a surface-attached PZT sensor. As sample 5 was already cracked in three-point bending, the lower tension zone was expected to have less strength under compressive loading than the upper compression zone. Therefore, cracks from the compression loading appeared firstly at the already cracked side, the notched side, as is evident from Figure 15 (a) & (b). The experiment was stopped once visible signs of spalling appeared, as shown in Figure 15.

3.6.1 Impedance signature response to compressive loading:

Figure 16 (a), (b), (c) and (d) show three main stages on the impedance signature through the progressive compressive loading. At stage A, an increasing shift for the impedance signature peaks' frequencies was observed as the loading increased. This shift can be noticed by considering the low-frequency range impedance signature which is shown in Figure 16 (a).

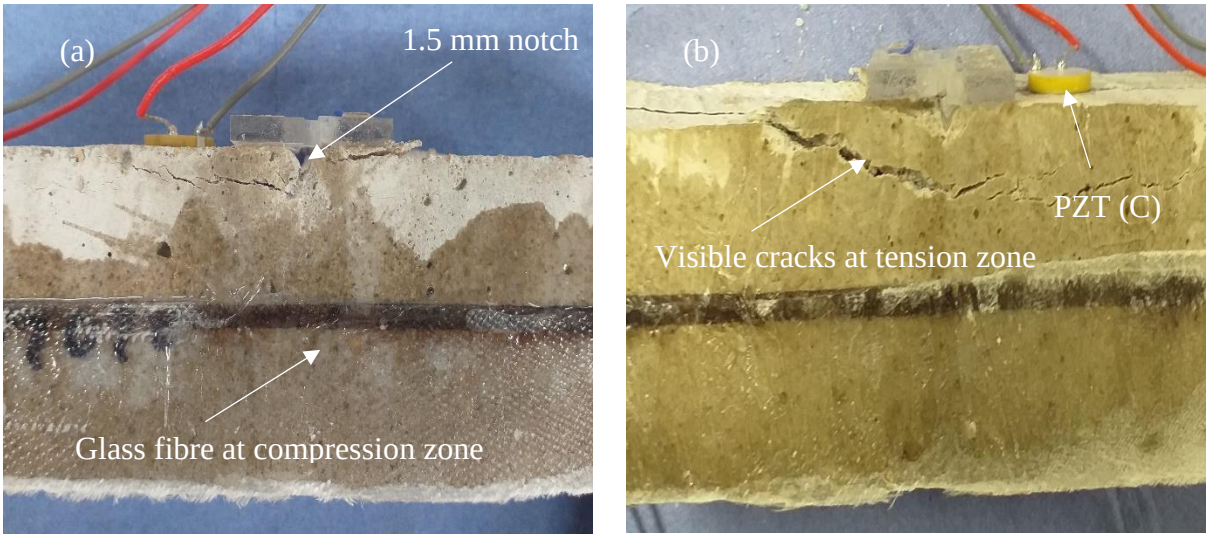

Figure 15: Near surface cracks due to compressive loading application on sample number 5, shown at (a) the front side of the sample, and (b) at the back side of the sample.

In this frequency range, increasing the loading values from 3 kN to 21 kN, shifts the impedance signature peak from 39.8 kHz. to 41.5 kHz. This shift is also evident at the other higher frequency ranges, shown in Figure 16 (b)-(d). Figures 17 (a)-(c), highlight the impedance signature response at different loading stages at the same frequency ranges shown in Figures 16 (b)-(d) for better clarity.

At stage B, the impedance signature peak frequencies started to follow a gradual constant trend. This constant trend for most of the assessed frequency ranges halted once the loading reached 39 kN. At stage C, which started at a loading value of 39 kN, a sudden change in the impedance

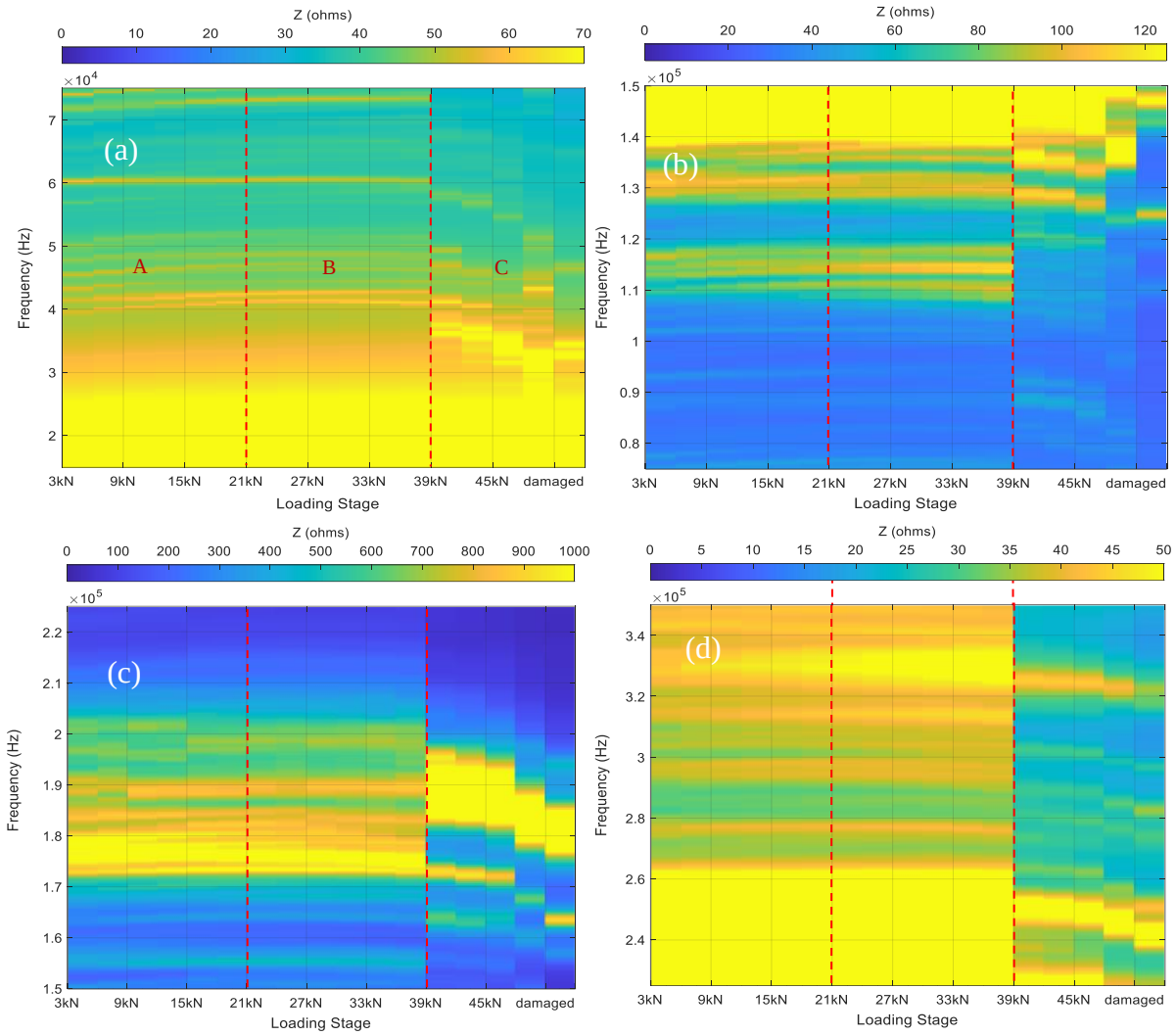

Figure 16: Impedance signature response for pre-cracked sample, through different compressive loadings stages at the frequency ranges of (a)15-75kHz, (b) 75-150kHz, (c) 150-225kHz, and (d) 225-350kHz.

signature shape occured, as defined high amplitude peaks developed, and a shift to a lower frequency range was observed as also shown in Figure 17.

The increase in the impedance signature peak frequency at stage (A), suggests an increase in the sample stiffness. due to filling of the voids, i.e. in this case crack closure, which increased the efficiency of loads transmission through the sample. As the crack closed through increased loading, the stiffness increasing rate decreased in the sample; therefore, stage (B) showed an almost constant impedance signature peak frequency.

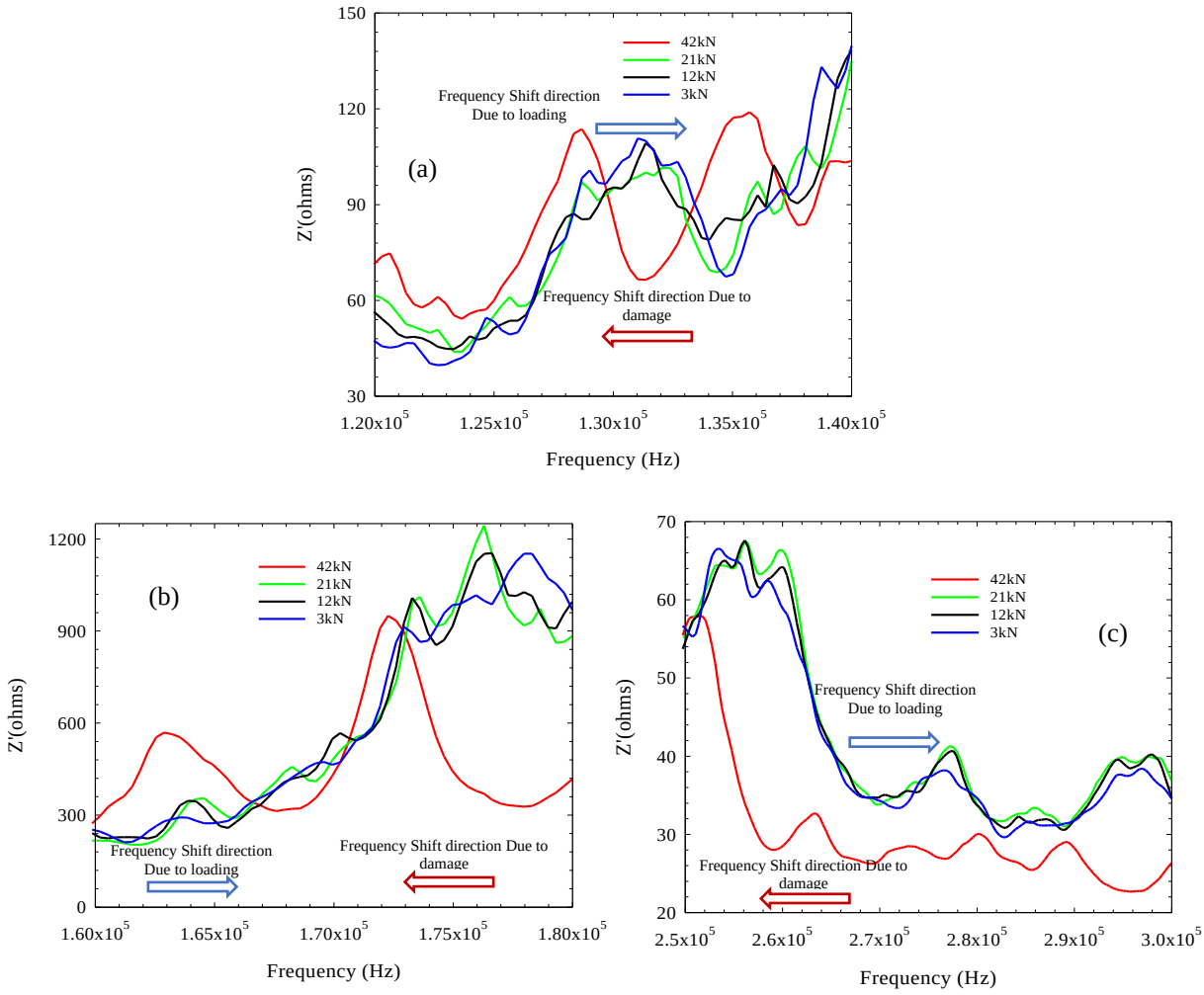

Figure 17: Selected impedance signatures for different loading values through the compressive loading for sample 5, at the frequency ranges of: (a) 120 – 140 kHz, (b) 160 – 180 kHz and (c) 250 – 300 kHz.

This trend continued until stage (C), as the impedance signature peaks frequency started to decrease, indicating a reduction in the sample stiffness, due to the initiation of microcracking in the sample.

From the above results, it is suggested that the crack closure process is associated with an increase in the stress in the sample; therefore, crack closure is expected to take place in the sample as early as stage A.

3.6.2 Damage metrics response to compressive loading:

Figure 18 shows the response of both the *Rmod (Z)* and *d(Z)* through different compressive loading stages and frequency intervals for sample 5. Both the *Rmod (Z)* and *(dZ)* in Figure 18

were normalised against their 3 kN loading stage value to account for the sensitivity difference between the different frequency ranges.

From Figure 18 (a) and (b), the *Rmod (Z)* showed high sensitivity to loads greater than 30 kN, especially at the frequency intervals of 15-65 kHz and 215-265 kHz. With regard to the *Rmod (dZ)* response, while the frequency intervals of 15-65 kHz and 65-115 kHz showed an increasing trend as the compressive loading increased, the 165-215 kHz and the 215-265 kHz, *Rmod (dZ)* showed a decreasing trend, which can be considered as an indication of the recovery of mechanical properties at initial loadings i.e. > 15 kN.

These observations would suggest that the *Rmod (dZ)* is able to highlight and detect the increase in loading through lower frequency ranges, while the crack closure was detected through the higher frequency ranges.

To further investigate the *Rmod (Z)* and *(dZ)* responses at early compressive loadings at the frequency intervals of 165-215 kHz and 215-265 kHz, Figure 19 shows the response of both the *Rmod (Z)* and *(dZ)* at loading values between 3 kN and 30 kN at the mentioned frequency ranges. The CMOD values were also plotted on the same graphs for comparison. Both the *Rmod (Z)* and *(dZ)* in Figure 19 were normalised against their first loading stage values to account for the difference in the sensitivity of the different frequency intervals.

For the COMD response in Figure 19, three different stages can be distinguished. At loading stages from 3 kN to 5 kN, there was a rapid increase in the CMOD response, before a reduction in the rate of increase between 5 kN and 15 kN. After this, the CMOD values continued to increase at a constant rate.

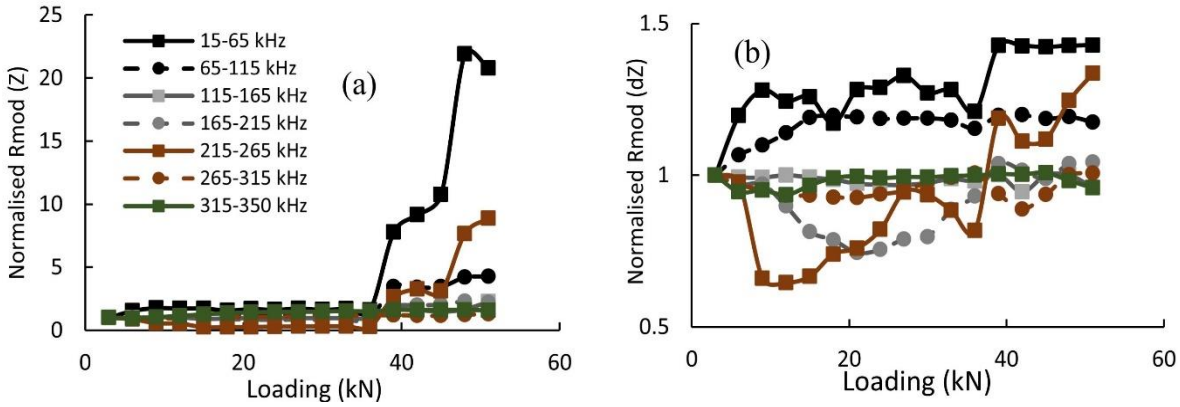

Figure 18: (a): *Rmod (Z)* and (b): *Rmod (dZ)* response through compressive loading increase estimated at different frequency ranges. Legend is shown in (a)

With regard to the *Rmod (Z)* and *(dZ)* responses in Figure 19, both of them show at first a decreasing trend before an increasing trend take place. The 215-265 frequency interval shows these different trends more clearly.

From these results, for both the CMOD and the damage metrics values, it is evident that most of the crack closure occured at early loading stages, i.e. between the loading values of 3 and 5 kN ,which is comparable in terms of the stress induced by shape memory polymers on pre-cracked cementiouse mortars [53], as a rapid increase in the CMOD is witnessed at this loading period. This early crack closure will cause coalescence of the crack edges, increasing stresses through the sample hence increasing the sample stiffness. Therefore, an increase in the resonant frequency in this stage occurs, and a reduction on both the *Rmod (Z)* and *d(Z)* values take place. After the coalescence between the crack edges, the stiffness in the sample starts to increase at a slower rate, as now the stiffness increase depends on filling the remaining voids in the crack vicinity or the sample in general. Therefore, the increase in both the resonant frequency and the CMOD values as well as the decrease in the damage metrics, starts to slow down.

After the loading value exceeds 15 kN, the CMOD values start to reflect the displacement in the sample at the notch vicinity. Therefore, at this stage, the stress in the sample increases,

which is reflected in the increase in the damage metric values, which indicates an increase in both the loading level and the damage level in the sample.

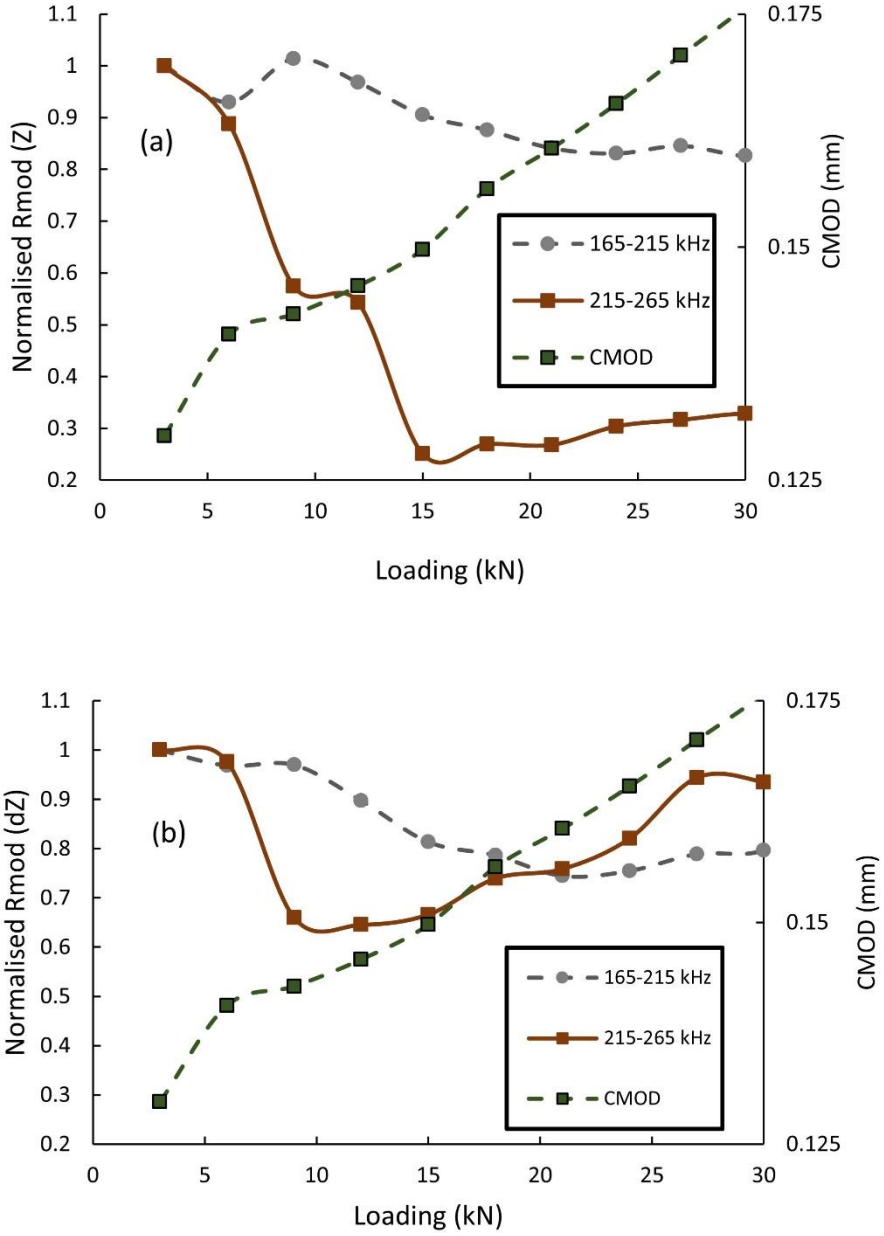

Figure 19: (a) *Rmod (Z)* response and (b) *Rmod (dZ)* response through different loading values and frequency ranges.

This increasing trend in the damage metrics and the CMOD continued until the measurements were stopped once visible signs of spalling were observed.

From the above results, it can be concluded that the PZT sensors are able to give an indirect indication of crack closure by detecting the increase in stress through the sample once a decrease in the crack width takes place.

4. **Conclusion:**

In this study, the effect of loading, cracking and crack-closure of mortar samples, on the electrical impedance signature of surface attached PZT sensors was studied.

Two scenarios were investigated throughout this study: a cracking scenario induced with a three-point bending experiment, and a crack closure (healing) scenario induced with compressive loading.

For the three-point bending cracking scenario, the impedance signature of the PZTs was shown to be sensitive to changes due to loading, especially at the lower frequency range. Once cracks occurred, both low-frequency and high-frequency ranges of the impedance signature were affected by exhibiting a shift in their peak values to lower frequency ranges.

By using the first difference of the impedance signature rather than the impedance signature, greater deviation for the loading and cracking stages from the pristine stage was detected, which suggested that the first difference of the impedance signature is more sensitive to changes in the mechanical properties during loading and damage. A sigmoidal relation was observed between the first difference and the impedance signature-based estimated damage metrics, which showed three discernible regions, which were related to the progressive reduction in the stiffness as the load increases on the sample.

Also, for different estimated damage metrices, low-frequency damage metrics showed to be more sensitive to far away damage and vice versa.

Subjecting the pre-cracked samples to compressive loading to simulate crack closure induced different responses on the impedance signature. At lower loading values, a shift in the impedance signature to higher frequency ranges was observed. As the loading increased, this shifting rate decreases, and at higher loads values, a shift to a lower frequency range was observed. When comparing these stages with the damage metrics responses and the CMOD results, these stages were related to the increase in the sample stress due to crack edges coalescence, increasing displacement in the notch vicinity due to crack closure, and due to damage initiation at higher compressive loads.

This research has demonstrated the ability of PZT type piezoceramic to identify both crack opening (an indication of damage to a concrete beam) and crack closure (an indication of healing which can improve durability).

CRediT authorship contribution statement

Hussameldin M. Taha: Conceptualization, Methodology, Validation, Formal analysis, Investigation, Writing - Original Draft, Visualization. **Richard J. Ball**: Conceptualization, Writing - Review & Editing, Supervision, Project administration, Funding acquisition. **Andrew Heath**: Conceptualization, Writing - Review & Editing, Funding acquisition.

Kevin Paine*:* Conceptualization, Writing - Review & Editing, Supervision, Project administration, Funding acquisition.

Acknowledgements

This research was funded by UK-EPSRC, grant number No. EP/P02081X/1, Resilient Materials 4 Life, RM4L. The authors gratefully acknowledge the Technical staff within Department of Architecture and Civil Engineering at the University of Bath for technical support and assistance in this work.

All data created during this research is openly available from the University of Bath Research Data Archive at : *Dataset for 'Crack growth and closure in cementitious composites: monitoring using piezoceramic sensors'.* Bath: University of Bath Research Data Archive. https://doi.org/10.15125/BATH-01039.

References:

[1] Gambhir, M.L., Concrete technology: theory and practice. 2013: Tata McGraw-Hill Education.

[2] Humphreys, K. and M. Mahasenan, Towards a sustainable cement industry. Substudy 8: climate change. 2002.

[3] Flower, D.J. and J.G. Sanjayan, Green house gas emissions due to concrete manufacture. The international Journal of life cycle assessment, 2007. 12(5): p. 282-288.

[4] Benhelal, E., et al., Global strategies and potentials to curb CO2 emissions in cement industry. Journal of Cleaner Production, 2013. 51: p. 142-161.

[5] Maddalena, R., H. Taha, and D. Gardner, Self-healing potential of supplementary cementitious materials in cement mortars: Sorptivity and pore structure. Developments in the Built Environment, 2021. 6: p. 100044.

[6] Alazhari, M., et al., Application of expanded perlite encapsulated bacteria and growth media for self-healing concrete. Construction and Building Materials, 2018. 160: p. 610-619.

[7] Giannaros, P., A. Kanellopoulos, and A. Al-Tabbaa, Sealing of cracks in cement using microencapsulated sodium silicate. Smart Materials and Structures, 2016. 25(8): p. 084005.

[8] Minnebo, P., et al., A Novel Design of Autonomously Healed Concrete: Towards a Vascular Healing Network. Materials, 2017. 10(1): p. 49.

[9] Davies, R.E., et al., A novel 2D vascular network in cementitious materials. 2015.

[10] Teall, O., et al., A shape memory polymer concrete crack closure system activated by electrical current. Smart Materials and Structures, 2018. 27(7): p. 075016.

[11] Davies, R., et al., Large Scale Application of Self-Healing Concrete: Design, Construction, and Testing. Frontiers in Materials, 2018.

[12] Paine, K., B. Reeksting, and H.T. and Susanne Gebhard. Integrating Self-Sensing in Self-Healing Concrete: Towards a Biomimetic Approach to Repair. in XV International Conference on Durability of Building Materials and Components (DBMC 2020). 2020.

[13] Park, S., et al., Multiple crack detection of concrete structures using impedance-based structural health monitoring techniques. Experimental Mechanics, 2006. 46(5): p. 609-618.

[14] Chaudhry, Z.A., et al. Local-area health monitoring of aircraft via piezoelectric actuator/sensor patches. in Smart Structures and Materials 1995: Smart Structures and Integrated Systems. 1995. International Society for Optics and Photonics.

[15] Park, G., et al., Impedance-based structural health monitoring for temperature varying applications. JSME International Journal Series A Solid Mechanics and Material Engineering, 1999. 42(2): p. 249-258.

[16] Song, G., et al., Concrete structural health monitoring using embedded piezoceramic transducers. Smart Materials and Structures, 2007. 16(4): p. 959.

[17] Sun, F.P., et al. Automated real-time structure health monitoring via signature pattern recognition. in Smart Structures and Materials 1995: Smart Structures and Integrated Systems. 1995. International Society for Optics and Photonics.

[18] Bhalla, S. and C. Kiong Soh, Structural impedance-based damage diagnosis by piezo-transducers. Earthquake Engineering & Structural Dynamics, 2003. 32(12): p. 1897-1916.

[19] Liang, C., F.P. Sun, and C.A. Rogers, Coupled Electro-Mechanical Analysis of Adaptive Material Systems-Determination of the Actuator Power Consumption and

System Energy Transfer. Journal of Intelligent Material Systems and Structures, 1997. 8(4): p. 335-343.

[20] Pan, H.H. and M.-W. Huang, Piezoelectric cement sensor-based electromechanical impedance technique for the strength monitoring of cement mortar. Construction and Building Materials, 2020. 254: p. 119307.

[21] Wang, D., H. Song, and H. Zhu, Embedded 3D electromechanical impedance model for strength monitoring of concrete using a PZT transducer. Smart Materials and Structures, 2014. 23(11): p. 115019.

[22] Su, Y.-F., et al., Novel methodology on direct extraction of the strength information from cementitious materials using piezo-sensor based electromechanical impedance (EMI) method. Construction and Building Materials, 2020. 259: p. 119848.

[23] Shin, S.W., et al., Piezoelectric sensor based nondestructive active monitoring of strength gain in concrete. Smart Materials and Structures, 2008. 17(5): p. 055002.

[24] Shin, S.W. and T.K. Oh, Application of electro-mechanical impedance sensing technique for online monitoring of strength development in concrete using smart PZT patches. Construction and Building Materials, 2009. 23(2): p. 1185-1188.

[25] Narayanan, A., A. Kocherla, and K.V. Subramaniam, Embedded PZT sensor for monitoring mechanical impedance of hydrating cementitious materials. Journal of Nondestructive Evaluation, 2017. 36(4): p. 64.

[26] Tawie, R. and H.K. Lee, Monitoring the strength development in concrete by EMI sensing technique. Construction and Building Materials, 2010. 24(9): p. 1746-1753.

[27] Bhalla, S., Smart system based automated health monitoring of structures. 2001, Nanyang Technological University, School of Civil and Structural Engineering.

[28] Hu, X., H. Zhu, and D. Wang, A study of concrete slab damage detection based on the electromechanical impedance method. Sensors, 2014. 14(10): p. 19897-19909.

[29] Ghafari, E., et al., Evaluation the compressive strength of the cement paste blended with supplementary cementitious materials using a piezoelectric-based sensor. Construction and Building Materials, 2018. 171: p. 504-510.

[30] Zhang, C., et al., Real-time monitoring stiffness degradation of hardened cement paste under uniaxial compression loading through piezoceramic-based electromechanical impedance method. Construction and Building Materials, 2020. 256: p. 119395.

[31] Narayanan, A. and K.V. Subramaniam, Experimental evaluation of load-induced damage in concrete from distributed microcracks to localized cracking on electro-mechanical impedance response of bonded PZT. Construction and Building Materials, 2016. 105: p. 536-544.

[32] Xu, D., et al., Temperature and loading effects of embedded smart piezoelectric sensor for health monitoring of concrete structures. Construction and Building Materials, 2015. 76: p. 187-193.

[33] S. Bhalla and N. Kaur, Prognosis of low-strain fatigue induced damage in reinforced concrete structures using embedded piezo-transducers. International Journal of Fatigue, 2018. 113: p. 98-112.

[34] N. Kaur and S. Bhalla, Combined Energy Harvesting and Structural Health Monitoring Potential of Embedded Piezo-Concrete Vibration Sensors. Journal of Energy Engineering, 2015. 141(4): p. D4014001.

[35] Taha, H., R.J. Ball, and K. Paine, Sensing of Damage and Repair of Cement Mortar Using Electromechanical Impedance. Materials, 2019. 12(23): p. 3925.

[36] Kim, H., et al., Performance assessment method for crack repair in concrete using PZT-based electromechanical impedance technique. NDT & E International, 2019. 104: p. 90-97.

[37] N. Kaur, S. Bhalla, and S.C. Maddu, Damage and retrofitting monitoring in reinforced concrete structures along with long-term strength and fatigue monitoring using embedded Lead Zirconate Titanate patches. Journal of Intelligent Material Systems and Structures, 2019. 30(1): p. 100-115.

[38] L. Qin, et al., The application of 1–3 cement-based piezoelectric transducers in active and passive health monitoring for concrete structures. Smart Materials and Structures, 2009. 18(9): p. 095018.

[39] N.P. Kaur, et al., Healing fine cracks in concrete with bacterial cement for an advanced non-destructive monitoring. Construction and Building Materials, 2020. 242: p. 118151.

[40] L. Tan, et al., Effect of carbonation on bacteria-based self-healing of cementitious composites. Construction and Building Materials, 2020. 257: p. 119501.

[41] Bascoul, A. and A. Turatsinze, Microstructural characterization of mode I crack opening in mortar. Materials and Structures, 1994. 27(2): p. 71.

[42] Batis, G., et al., The effect of metakaolin on the corrosion behavior of cement mortars. Cement and Concrete Composites, 2005. 27(1): p. 125-130.

[43] Chen, X., S. Wu, and J. Zhou, Influence of porosity on compressive and tensile strength of cement mortar. Construction and Building Materials, 2013. 40: p. 869-874.

[44] EN197-1:2011, in Cement: Composition, specifications and conformity criteria for common cements. 2011, BSI: London, UK.

[45] BSI, BS EN 196-1: 2005: Methods of testing cement. Determination of strength. 2005, BSI London, UK.

[46] PI_Piezo_Technology. Piezoelectric Materials n.d [cited 2021 23.5.2021]; Available from: https://www.piceramic.com/en/products/piezoelectric-materials/#c15163.

[47] C.-W. Ong, et al., Application of the electromechanical impedance method for the identification of in-situ stress in structures. SPIE's International Symposium on Smart Materials, Nano-, and Micro- Smart Systems. Vol. 4935. 2002: SPIE.

[48] V.G.M. Annamdas, Y. Yang, and C.K. Soh, Influence of loading on the electromechanical admittance of piezoceramic transducers. Smart Materials and Structures, 2007. 16(5): p. 1888-1897.

[49] Y. Yang, Y.Y. Lim, and C.K. Soh, Practical issues related to the application of the electromechanical impedance technique in the structural health monitoring of civil structures: II. Numerical verification. Smart Materials and Structures, 2008. 17(3): p. 035009.

[50] Y. Yang, Y.Y. Lim, and C.K. Soh, Practical issues related to the application of the electromechanical impedance technique in the structural health monitoring of civil structures: I. Experiment. Smart Materials and Structures, 2008. 17(3): p. 035008.

[51] Toumi, A., A. Bascoul, and A. Turatsinze, Crack propagation in concrete subjected to flexuralcyclic loading. Materials and Structures, 1998. 31(7): p. 451-458.

[52] Petersson, P.-E., Crack growth and development of fracture zones in plain concrete and similar materials. 1981.

[53] A. Jefferson, et al., A new system for crack closure of cementitious materials using shrinkable polymers. Cement and Concrete Research, 2010. 40(5): p. 795-801.